

ARTICLE

DOI: 10.1038/s41467-018-02836-6

OPEN

Measurements of growing surface tension of amorphous–amorphous interfaces on approaching the colloidal glass transition

Divya Ganapathi¹, K. Hima Nagamanasa^{2,5}, A.K. Sood^{1,3} & Rajesh Ganapathy^{3,4}

There is mounting evidence indicating that relaxation dynamics in liquids approaching their glass transition not only become increasingly cooperative, but the relaxing regions also become more compact in shape. Of the many theories of the glass transition, only the random first-order theory—a thermodynamic framework—anticipates the surface tension of relaxing regions to play a role in deciding both their size and morphology. However, owing to the amorphous nature of the relaxing regions, even the identification of their interfaces has not been possible in experiments hitherto. Here, we devise a method to directly quantify the dynamics of amorphous–amorphous interfaces in bulk supercooled colloidal liquids. Our procedure also helped unveil a non-monotonic evolution in dynamical correlations with supercooling in bulk liquids. We measure the surface tension of the interfaces and show that it increases rapidly across the mode-coupling area fraction. Our experiments support a thermodynamic origin of the glass transition.

¹Department of Physics, Indian Institute of Science, Bangalore 560012, India. ²Chemistry and Physics of Materials Unit, Jawaharlal Nehru Centre for Advanced Scientific Research, Jakkur, Bangalore 560064, India. ³International Centre for Materials Science, Jawaharlal Nehru Centre for Advanced Scientific Research, Jakkur, Bangalore 560064, India. ⁴Sheikh Saqr Laboratory, Jawaharlal Nehru Centre for Advanced Scientific Research, Jakkur, Bangalore 560064, India. ⁵Present address: IBS Center for Soft and Living Matter, UNIST, Ulsan 689-798, South Korea. Correspondence and requests for materials should be addressed to D.G. (email: divyaganaka@gmail.com) or to R.G. (email: rajeshg@jncasr.ac.in)

The precise mechanisms by which liquids vitrify, upon rapid cooling, continue to elude our grasp^{1–3}. Of the many competing theories, both thermodynamic^{4–8} and kinetic^{9–11}, that attempt to capture the dynamical slowing down during glass formation, the well-developed thermodynamic framework of random first-order theory (RFOT) has recently gained prominence. RFOT anticipates two transitions en route to forming glass^{1,12}. The first, a purely dynamical transition at $T_c > T_K$ (T_c and T_K being the mode-coupling and Kauzmann temperatures, respectively) is associated with the fragmentation of the homogeneous liquid into a patchwork of distinct amorphous mosaics, separated by well-defined interfaces. The competition between the configurational entropy gain and the interfacial energy cost following a rearrangement sets the size of these mosaics, which in turn governs the structural relaxation time, τ_α . With further supercooling, the mosaic size is expected to grow and eventually diverge at a bona fide thermodynamic transition to an ideal glass at T_K ^{1,3}. A non-zero surface tension, Υ , is essential for the stability of these mosaics^{13–15} and is perhaps the most fundamental prediction of RFOT. Nevertheless, even identifying these interfaces, let alone quantify the evolution of Υ across T_c , has not been possible in bulk liquids. Instead, motivated by measurements of the mosaic size, also called the point-to-set length ξ_{PTS} , in particle pinning based methods¹⁶, theoretical and numerical studies have attempted to use this method to quantify Υ ^{13,14,17} and also probe the statistics of interface fluctuations^{15,16,18}. While Υ was estimated to grow monotonically across T_c , the study focused on inherent structures and moreover measuring Υ also involved swapping particles within a cavity keeping the boundary ones frozen and hence has no experimental analogue¹³. Simulations that probed the dynamics of a liquid near a pinned amorphous wall have also uncovered direct evidence for the predicted change in relaxation mechanism across T_c ¹⁹, in terms of a maximum in the dynamic correlation length, ξ_d ²⁰. Subsequent colloid experiments that mimicked the simulation protocol not only corroborated these findings but also showed that the maximum in ξ_d coincides with the change in shape of most-mobile particle clusters from string like to compact^{21,22}. This observation was at odds with the dynamical facilitation theory of glasses^{2,11}.

Even while the artificial introduction of disorder by pinning particles seems to be a prerequisite for testing predictions from RFOT^{13–16,20,21,23–26}, whether these findings readily carry over to structural glasses, where disorder is self-pinned¹, remains unanswered. At present, even in numerical studies on bulk supercooled liquids, evidence for a change in relaxation dynamics across T_c is rather indirect^{27,28} leading to suggestions that the non-monotonicity in ξ_d may be unique to the pinned wall geometry^{29–31}. These concerns notwithstanding, simulations find that a pinned wall can subtly influence particle dynamics by exerting entropic forces that depend on the nature of the interparticle potential³². Similar problems persist even when the particles are randomly pinned. Although increasing the concentration of the pins results in a substantial growth in τ_α , the peak in the dynamic susceptibility, χ_4^* , related to the size of dynamical heterogeneities, remains nearly constant³³ or is found to decrease³⁴ depending on the system under consideration. This behavior of χ_4^* is unlike what is observed in bulk liquids, where it steadily grows with supercooling, and suggests that the nature of relaxation dynamics in the pinned liquid may be quite different from the bulk. Dynamics aside, there is no consensus on whether ξ_{PTS} is even order agnostic and tracks structural correlations that are different from those obtained from simple pair-correlations^{35,36}. Developing strategies to help resolve these controversies is a much needed step towards solving the glass transition puzzle.

Using the data acquired from optical video microscopy experiments on bulk supercooled colloidal liquids (see Methods section for details), here we devise a novel scheme to identify self-induced pins and probe their influence on local structure and dynamics. We exploit this conceptual advance to side step controversies surrounding the pinning procedure and directly measure the surface tension of the interfaces delineating regions of high and low configurational overlap. Apart from a growing static length scale, we also observe a non-monotonic evolution in the dynamic length scale, with supercooling, even in the absence of externally introduced pinning. Using the capillary fluctuation method (CFM)^{37–41}, we calculate the surface tension of the interfaces and show that it grows rapidly on approaching the mode-coupling area fraction as anticipated by RFOT.

Results

Evolution of length scales in bulk colloidal glass formers. We identify self-induced pins by exploiting the fact that τ_α is determined by the slowest relaxing regions in the supercooled liquid and hence regions that harbor these pins should also be configurationally similar over at least τ_α . The configurational overlap $q_c(t)$ which measures the extent of this similarity over time is also thought to be the order parameter within RFOT^{1,12}. We measure $q_c(t)$ by first coarse-graining the field of view into boxes of size $1\sigma_s$ (Fig. 1a). The box size is optimally chosen to minimize the overlap fluctuations due to cage rattling as well as avoid multiparticle occupancy in a given box^{20,21}. Nevertheless, particles located near the box edges can still hop to neighboring boxes and this results in spurious overlap fluctuations. We account for these by developing the fuzzy-grid method which involves displacing the coarse-graining grid by the cage size $0.1\sigma_s$ in various directions and then averaging $q_c(t)$ obtained from each of the realizations (Supplementary Note 1 and Supplementary Fig. 1). For each box and for $t = \tau_\alpha$ we compute $q_c(t) = \frac{\langle n_i(t)n_i(0) \rangle_t}{\langle n_i(0) \rangle_t}$, where i is the box index, $n_i(t) = 1$ if the box contains a particle at time t and $n_i(t) = 0$ otherwise. Unlike the case of the quenched disorder, self-induced pins do not persist indefinitely since the liquid eventually relaxes and hence the time averaging denoted by $\langle \rangle_t$ is performed over $1\tau_\alpha$. Boxes with a $q_c(\tau_\alpha) > 0.9$ are identified as self-induced pins (red box in Fig. 1a and Supplementary Fig. 2) and we restrict our attention to those that persisted over many consecutive τ_α 's. For $\phi = 0.79 > \phi_{\text{MCT}}$, however, owing to experimental difficulties with sample equilibration, $t = 7t^*$, where t^* is the cage-breaking time^{21,42} (Supplementary Fig. 3).

Having identified the pins, we probe their influence on local static order and dynamics by adapting the procedure originally developed for the amorphous wall geometry²⁰. In order to improve the spatial resolution, the coarse-graining box size was lowered to $0.5\sigma_s$. Next, we compute the radially averaged configurational overlap $q_c(t,r) = \langle q_c(t) \rangle_r$ and the self-overlap $q_s(t,r) = \frac{\langle n_i^2(t)n_i^2(0) \rangle_t}{\langle n_i^2(0) \rangle_t}$ for all boxes at a distance r from a given pin. Here, $n_i^2(t) = 1$ if the box is occupied by the same particle at time t and $n_i^2(t) = 0$ otherwise. By construction, $q_c(t,r)$ is insensitive to particle swaps, while $q_s(t,r)$ is sensitive. Figure 1b shows the time evolution of $q_c(t,r)$ for $\phi = 0.74$ at different r 's. The long time value of $q_c(t \rightarrow \infty, r) = q_\infty$ is proportional to the extent to which self-induced pins influence the local static density field. We obtain q_∞ by averaging over the plateau region of $q_c(t,r)$ (horizontal lines in Fig. 1b). For large r 's, as expected, q_∞ hovers around the bulk value $q_{\text{rand}} = q_\infty(r \rightarrow \infty)$ (dashed line in bottom panel of Fig. 1c). Here, q_{rand} measures the probability that a box is occupied. For small r , however, we observe oscillations in q_∞ centered around q_{rand} . By the very definition of $q_c(t,r)$, we expect q_∞ for r 's corresponding to predominantly filled(empty)

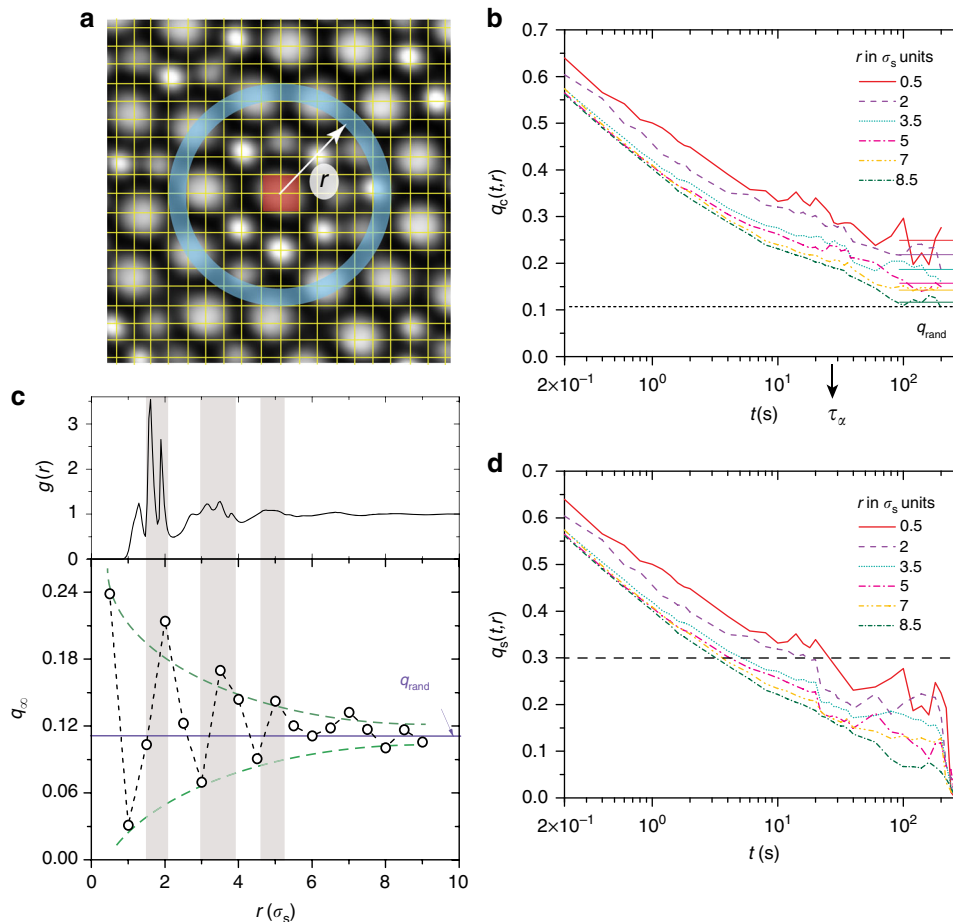


Fig. 1 Configurational and self-overlap around self-induced pins. **a** The background image represents a small portion of the field of view of a colloidal supercooled liquid. The grid corresponds to a box size of $0.5\sigma_s$. The red box in the center of the image represents a self-induced pin with $q_c(\tau_\alpha) > 0.9$ over a $1\sigma_s$ box size. Upon fine-graining to $0.5\sigma_s$ boxes to improve the spatial resolution, the overlap of the self-induced pin is shared by four boxes within the red region. $\langle q_c(t) \rangle_r$ is obtained by radially averaging boxes at a distance r (blue ring) from the center. **b** Time evolution of configurational overlap $q_c(t,r)$ for $\phi = 0.74$ at different r 's from the self-induced pin. The horizontal line dashed line represents the random occupancy in the bulk q_{rand} . **c** Top panel shows $g(r)$ for the binary supercooled liquid at $\phi = 0.74$ and the bottom panel shows the evolution of q_∞ around a self-induced pin. The purple line corresponds to the bulk value q_{rand} . The green lines are only a guide to the eye. For the sake of clarity, **b** shows $q_c(t,r)$ only for r 's where $q_\infty > q_{rand}$. **d** Time evolution of self-overlap $q_s(t,r)$ for $\phi = 0.74$ at different distances (σ_s) from the self-induced pin. The horizontal red dashed line corresponds to $q_s(t,r) = 0.3$

boxes to be larger(smaller) than q_{rand} . Not surprisingly, the maxima and minima in q_∞ coincide with those observed in the pair-correlation function, $g(r)$, and indeed correspond to predominantly filled and empty coordination shells around the self-induced pin (top panel of Fig. 1c). The oscillations thus reflect the local liquid-like order around the pin and grow in amplitude on nearing the pin and indicate that density fluctuations become increasingly frozen. Since $q_c(t,r)$ is a measure of persistence of configurations, the oscillations in q_∞ are more stark even at large r in comparison to $g(r)$ —a purely static measure. Unlike $q_c(t,r)$, $q_s(t,r)$ decays to zero in the long time limit, when particles have undergone displacements larger than the box size (Fig. 1d). We define the relaxation time $\tau_s(r)$ as the time taken for $q_s(t,r)$ to decay to 0.3. For all ϕ 's, the lifetime of the self-induced pins considered is larger than $\tau_s(r)$ and the pins therefore mimic quenched random disorder. As expected, $\tau_s(r)$ close to the pin is larger than its bulk value τ_s^{bulk} .

Analogous to the behavior of static correlations in liquids with externally introduced pins^{20,21,23}, the excess contribution to the configurational overlap over the bulk, $|q_\infty(r) - q_{rand}|$, decays exponentially with r for all ϕ 's even for self-induced pins (Fig. 2a).

This allowed us to estimate a static correlation length ξ_{stat} from the relation $|q_\infty(r) - q_{rand}| = B \exp(-r/\xi_{stat})$. As seen in simulations and experiments, we observe that the prefactor B depends on ϕ ^{20,21}. We explicitly account for this dependence by defining a second static length scale $\xi_{stat-int} = B \xi_{stat}$ ²⁰. We next attempted to extract the dynamic length scale ξ_d . In Fig. 2b, we show $\ln(\tau_s(r)/\tau_s^{bulk})$ versus r for different ϕ 's. For all ϕ 's except $\phi = 0.76$ (inverted red triangles in Fig. 2b), $\ln(\tau_s(r)/\tau_s^{bulk})$ shows an exponential decay. For $\phi = 0.76$, which is close to the mode-coupling area fraction ($\phi_{MCT} = 0.77$, Supplementary Fig. 4), however, we clearly see two slopes. A similar departure from an exponential decay has been observed in the presence of a pinned amorphous wall^{20,21} and was attributed to the presence of multiple relaxation processes near the MCT transition¹⁹. We extract ξ_d from the relation $\ln(\tau_s(r)/\tau_s^{bulk}) = B_s \exp(-r/\xi_d)$ ²⁰.

We perform the equivalent of disorder averaging by repeating the above analysis for at least 6–8 pins (≈ 12 pins are used in calculating ξ_d for $\phi = 0.75-0.79$) within our field of view. We ensure that the average inter-pin separation is $> 10-12\sigma_s$. The small hollow triangles and circles in Fig. 2c correspond to ξ_{stat} and ξ_d evaluated for each of these pins and the larger symbols

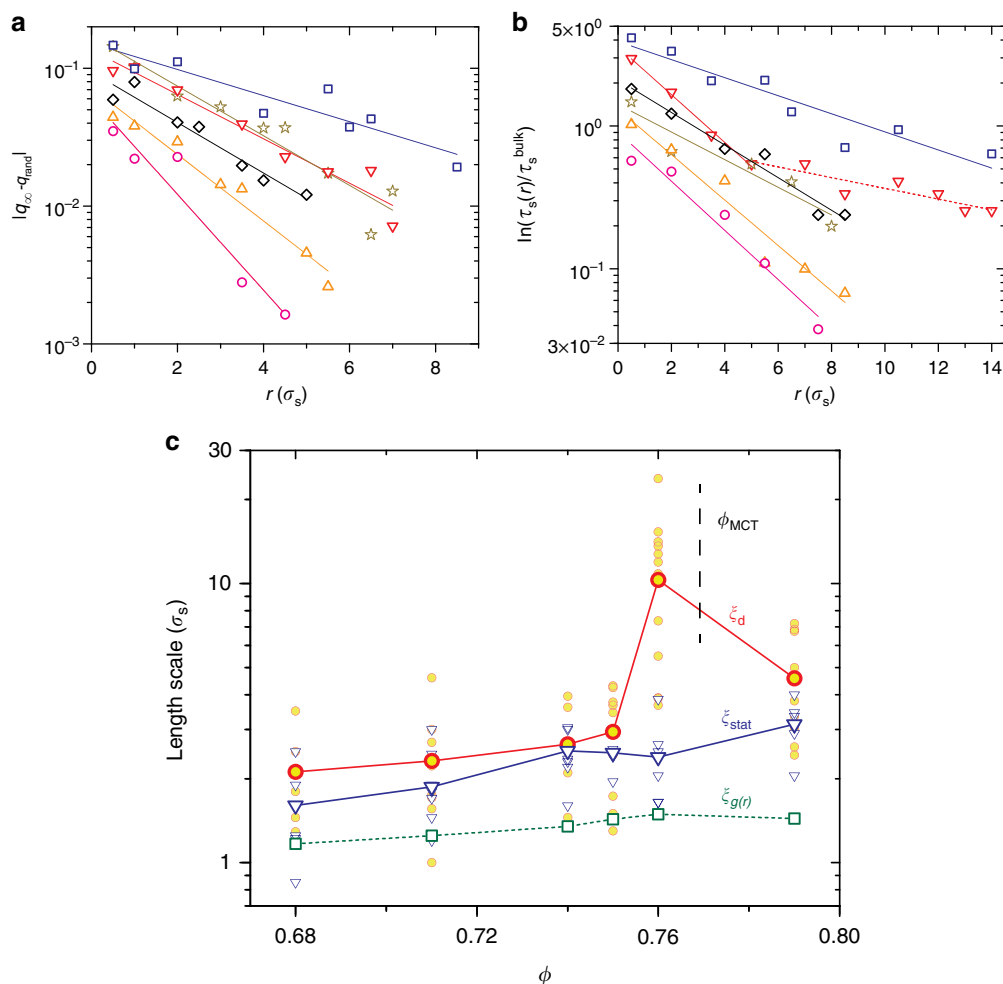


Fig. 2 Static and non-monotonic dynamic correlations in unpinned supercooled liquids. **a** and **b** correspond to $|q_\infty - q_{rand}|$ and $\ln(\tau_s(r)/\tau_s^{\text{bulk}})$ versus r , respectively. $\phi = 0.68$ (pink circles), $\phi = 0.71$ (orange triangles), $\phi = 0.74$ (gray diamonds), $\phi = 0.75$ (dark yellow stars), $\phi = 0.76$ (red inverted triangles), and $\phi = 0.79$ (blue squares). **c** The small circles and triangles represent ξ_d and ξ_{stat} , respectively, for many independent pins for a given ϕ and the larger symbols represent their averages. The squares correspond to the two-point correlation length. For $\phi = 0.76$, the asymptotic slope was used in calculating ξ_d

correspond to their averages for each ϕ (Supplementary Fig. 5). We also show the two-point correlation length $\xi_{g(r)}$ (hollow green squares) obtained by fitting an envelope to the decay of the pair-correlation function $g(r)$ for comparison. While ξ_{stat} appears to grow faster than $\xi_{g(r)}$, the more striking feature is the presence of a maximum in ξ_d . The observed trends are not very sensitive to the value of $q_c(\tau_\alpha)$ used to define a self-induced pin or issues with sample equilibration beyond ϕ_{MCT} (Supplementary Note 2 and Supplementary Figs. 6–10). This is the first observation of a non-monotonic evolution of a dynamic length scale in a bulk supercooled liquid. The presence of this maximum near ϕ_{MCT} is consistent with the change in shape of dynamical heterogeneities observed earlier²¹. Also, both ξ_{stat} and ξ_d for self-induced pins grow weaker than the amorphous wall geometry²¹. While this could simply be due to the lack of disorder averaging in the latter, simulations find that the length scales in the random pinning geometry, where the pin configuration is similar to the self-induced pinning case, evolve much more slowly than for other pin geometries²³ and are also consistent with theoretical predictions²⁵. Further, while the standard deviation in ξ_{stat} remains nearly same for all ϕ 's studied, for ξ_d it is maximal near ϕ_{MCT} (Supplementary Fig. 11) and this may be another signature of being in the vicinity of the dynamical crossover predicted by RFOT. More importantly, these observations unambiguously

show that the non-monotonic evolution of ξ_d , hitherto observed only in liquids in the presence of a pinned amorphous wall^{20,21}, is clearly a feature of the bulk liquid and is not an outcome of the pinning procedure as alluded in recent studies^{29,31}.

Identifying amorphous–amorphous interfaces. The striking similarities in the evolution of static and dynamic length scales between artificially introduced and self-induced pinning motivated us to explore if the methods for identifying amorphous–amorphous interfaces in the former can be extended to the latter^{13–15}. Since experimental studies of such interfaces are lacking even for pinned liquids, we first analyze data on colloidal liquids in the presence of an optically pinned amorphous wall²¹ (Supplementary Note 3 and Supplementary Fig. 12). We coarse-grain the field of view into $1\sigma_s$ boxes and subsequently calculate the persistence function $p_c(t = \tau_\alpha) = \langle p_i(t) \rangle$, where $p_i(t) = 1$ if the occupancy of box i remains unchanged at time $t = 0$ and $t = t$ and $p_i(t) = 0$ otherwise²⁷. The $\langle \rangle$ denotes averaging over $1\tau_\alpha$. This minor modification to the definition of $q_c(t)$ ensures that, post coarse-graining, an empty box in an immobile region of the liquid is treated on par with an occupied one. Figure 3a shows a snapshot of $p_c(\tau_\alpha)$ for $\phi = 0.75$. The image corresponds to the portion of the field of view that contains the wall located at $z \leq 0$

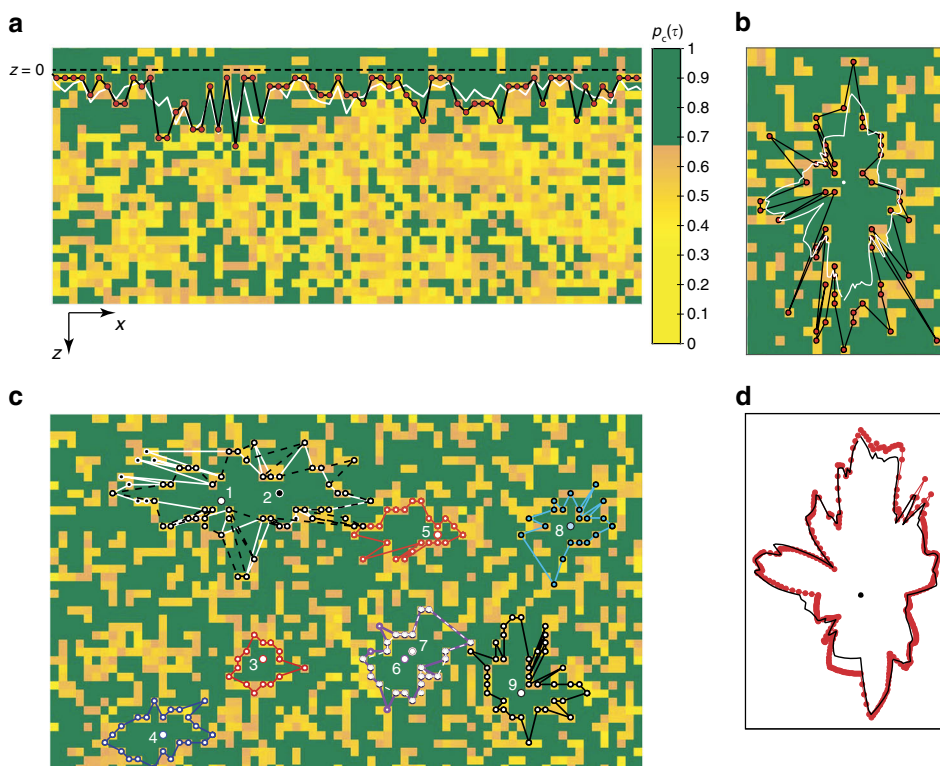


Fig. 3 Identifying amorphous-amorphous interfaces. **a** The background image represents the $p_c(\tau_\alpha)$ for a portion of the field of view containing the amorphous wall located at $z \leq 0$ (dashed line) for $\phi = 0.75$. The color bar represents $p_c(\tau_\alpha)$ values. The black line through the red symbols corresponds to the instantaneous interface profile $h(z,t)$ and the white line is the time-averaged profile $\langle h(z,t) \rangle_t$. **b** Interface profile around self-induced pin represented by the white circle. The background color scheme and the lines have the same meaning as in **a**. **c** Instantaneous interface profiles around distinct self-induced pins (represented by the numbered circles). Pins 1 and 2 and pins 6 and 7 lie within the same mosaic and yield nearly the same interface. **d** Instantaneous interface profile post fuzzy-grid averaging. The black line represents the $\langle h(z,t) \rangle_t$ around the pin (black circle). In **b-d**, $\phi = 0.79$

(dashed line). In line with expectations, $p_c(\tau_\alpha)$ for regions close to the wall ($z > 0$) is larger as compared to regions farther away from it (represented by green and yellow boxes, respectively). Next, starting from each box at $z=0$, we scan along z and locate the box where the overlap dropped to $p_c(\tau_\alpha) \leq 0.67$. The line joining these boxes delineates the regions of high and low configurational overlap^{14,15} and we define this to be the instantaneous interface profile, $h(z,t)$, for a given τ_α (black line in Fig. 3a). We follow this procedure for each τ_α and quantify the dynamics of $h(z,t)$ (Supplementary Note 4). We find that the time-averaged interface profile, $\langle h(z,t) \rangle_t$, as expected, is parallel to the wall at $z=0$ (white line in Fig. 3a). For each ϕ , interface fluctuations are probed over their corresponding τ_α and a direct comparison of their dynamics is thus possible. Supplementary Movies 1 and 2 show interface fluctuations for the pinned wall geometry for $\phi = 0.75$ and $\phi = 0.79$, respectively.

We made modifications to the above procedure for identifying interfaces around self-induced pins. Starting from the pin (represented as solid white circle in Fig. 3b), we scan along x and z directions for boxes where the overlap dropped to $p_c(\tau_\alpha) \leq 0.67$ (Supplementary Note 4 and Supplementary Fig. 13). A line through these boxes represents the instantaneous interface profile. Figure 3c shows the interfaces obtained from this procedure for many well-separated pins within our field of view for $\phi = 0.79$. At high ϕ 's especially, the regions with a high configurational overlap typically contain more than one self-induced pin (Supplementary Fig. 2). We have checked that the interface profile obtained starting from any of these pins defines nearly the same high overlap region (white and pink interface profiles around pins labeled 1 and 2 and 6 and 7, respectively, in

Fig. 3c). We then carry out the fuzzy-grid averaging procedure to smoothen out interface fluctuations for both the pinned wall and self-induced pins. The resulting interface profile is interpolated (black line through red symbols in Fig. 3d) before further analysis. Supplementary Movies 3 and 4 show interface fluctuations around self-induced pins for $\phi = 0.75$ and $\phi = 0.79$, respectively.

Growing surface tension of amorphous-amorphous interfaces.

The surface tension of an interface is inversely related to its roughness, which is best captured by the interface width $w = \sqrt{\langle \Delta h \rangle^2} = \sqrt{\langle h(z,t) - \langle h(z,t) \rangle_t \rangle^2}$ ³⁷⁻⁴¹. Since the amplitude of interface fluctuations is extensive in the system size and diverges in the thermodynamic limit, we only consider interfaces of the same length (Supplementary Note 5). Figure 4a and Supplementary Fig. 14a show the evolution in the distribution of height fluctuations, $P(\Delta h)$ with ϕ , for the self-induced pin and the pinned wall, respectively. $P(\Delta h)$ gets narrower with ϕ which already signals a growth in the γ of the high p_c regions. While $P(\Delta h)$ is well captured by Gaussian fits at low ϕ 's, we observe deviations for $\phi > 0.75$ and hence extract w by fitting a Gaussian only to the central region where $P(\Delta h)$ dropped by about a decade. In Fig. 4b, we show w versus ϕ for the self-induced pin (solid symbols) and the pinned wall (hollow symbols). Strikingly, for both these cases, we observe that w appears to taper off beyond ϕ_{MCT} .

Next, we attempt to measure γ directly using the CFM. CFM was originally developed to quantify the dynamics of flat interfaces separating phases with a well-defined order parameter³⁸⁻⁴¹, and it is not immediately apparent if this approach can be extended to

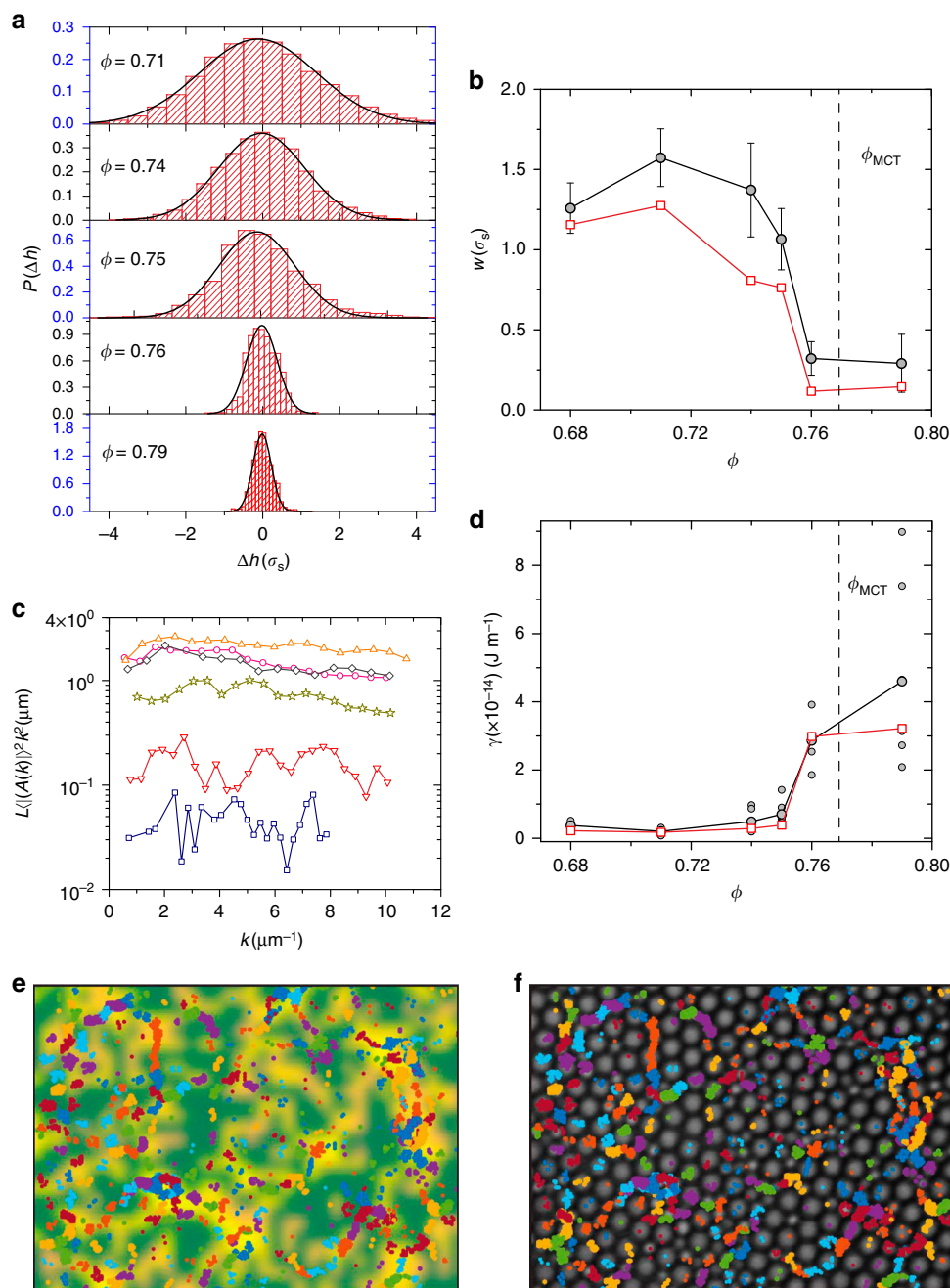


Fig. 4 Surface tension of amorphous-amorphous interfaces. **a** Normalized histogram of height fluctuations for various ϕ s. The black lines represent Gaussian fits to the data. **b** Interface width w versus ϕ for amorphous wall (hollow squares) and for self-induced pins (hollow circles). Error bars represent the standard deviation of w obtained from distinct self-induced pins. **c** $L(|A(k)|^2)k^2$ versus k for a representative self-induced pin. $\phi = 0.68$ (pink circles), $\phi = 0.71$ (orange triangles), $\phi = 0.74$ (gray diamonds), $\phi = 0.75$ (dark yellow stars), $\phi = 0.76$ (red inverted triangles), and $\phi = 0.79$ (blue squares). **d** The small hollow circles represent γ for distinct self-induced pins and the large circles represent their average for each ϕ . γ versus ϕ for amorphous wall (hollow squares). **e** The background image represents $p_c(t = 7t^*)$ for $\phi = 0.79$. **f** Snapshot of liquid configuration corresponding to **e**. In **e** and **f**, the trajectories of the top 1% most-mobile particles are shown by the colored symbols

configurational overlap fields and that too for interfaces that are curved like those seen around self-induced pins. At finite temperature, interfaces undergo broadening due to thermal fluctuations and the final equilibrium profile is a trade off between the surface energy term which prefers a flat interface and the thermal energy $k_B T$. In CFM, $h(z, t)$ is decomposed into normal modes and the amplitude of each mode decays as $\langle |A(k)|^2 \rangle = k_B T / LYk^2$ in accordance with the equipartition theorem. Here, k is the wavevector and L is the length of the interface. Figure 4c and Supplementary Fig. 14b show $L(|A(k)|^2)k^2$ versus k

as a function of ϕ for a representative self-induced pin and the pinned wall, respectively. We find that in both cases, $L(|A(k)|^2)k^2$ is constant for almost a decade in k which not only validates the applicability of CFM for the present system but also allowed us to quantify γ for the first time in experiments. Our findings are not very sensitive to the precise definition of the configurational overlap used, the coarse-graining box size, and the choice of time scale in defining the interface (Supplementary Notes 6 and 7 and Supplementary Figs. 15–21). Figure 4d shows γ versus ϕ for many well-separated self-induced pins (small gray circles) and the

pinned wall (hollow squares). The filled black circles correspond to the average γ for each ϕ . Remarkably, we observe that with supercooling, γ grows rather rapidly in the vicinity of ϕ_{MCT} .

In the original version of RFOT⁵, the concept of a mosaic state is not meaningful beyond the spinodal singularity where metastability is lost ($T > T_c$ regime), and hence γ is also expected to drop to zero above T_c ($\phi < \phi_{\text{MCT}}$ in colloid experiments). In our experiments, we not only find γ to be finite but it also grows as ϕ_{MCT} is approached from below (Supplementary Fig. 22). A generalized RFOT, proposed recently^{13,16}, suggests that the value of γ between distinct pairs of amorphous mosaics is not identical, as assumed earlier⁵, but is instead a broad distribution with only the average γ vanishing for $T \geq T_c$ ¹³. A broad distribution in γ implies that the mosaic state can survive in the $T > T_c$ regime and the sharp transition at T_c is thus smeared out. Theoretical arguments also anticipate that the distribution of activation energy barriers develop long tails near T_c , due to presence of secondary string-like relaxation processes, resulting in a smoothing of the transition⁴³. Thus, while a non-zero value of γ even at the lowest ϕ 's we study may simply be an outcome of our analysis procedure, the systematic growth in γ lends support to the generalized RFOT. Strikingly, the experimentally observed growth in γ is in accord with the expected¹⁹ and observed compaction of cooperatively relaxing regions (CRRs) on supercooling across ϕ_{MCT} ^{20,21}.

Anisotropic caging at amorphous–amorphous interfaces. We finally focus on the dynamics of most-mobile particles at amorphous–amorphous interfaces. In Fig. 4e, we show the top 1% of particles that were labeled most-mobile over a t^* interval⁴⁴ that fell within the time window ($7t^*$) over which the underlying $p_c(t)$ was calculated for $\phi = 0.79$. Figure 4f shows a snapshot of the liquid at the beginning of the $7t^*$ window. The different colors in Fig. 4e and f represent different particles. While it is not surprising that these particles are predominately found in the low p_c regions, we observe that for most particles the trajectories are elongated along the interface length. This anisotropic weakening of the cage should result in string-like CRRs oriented along the interface and is strikingly similar to the dynamics of particles at crystal grain boundaries⁴⁵.

Discussion

The novel scheme put forth here for identifying self-induced pins has helped unveil the existence of interfaces separating adjacent relaxing regions in bulk supercooled liquids. Although our experiments are restricted to the boundary of the RFOT regime ($\phi \sim \phi_{\text{MCT}}$) in order to avoid too large relaxation times, the observed rapid growth in the surface tension with supercooling is in line with theoretical expectations of a crossover between null amorphous surface tension and a finite one. Further, the non-monotonic evolution in ξ_d with ϕ finds a natural explanation only within the RFOT paradigm. Crucially, the fact that the static and dynamical length scales and interface dynamics in the bulk liquid mirror those seen in the pinned liquid strengthens numerous findings on the latter which favor a thermodynamic origin of the glass transition. Given that the involved procedure of artificially pinning particles is not essential to verify RFOT opens the door to extending our method to supercooled liquids made of particles with complex shapes and internal degrees of freedom. In the ongoing quest for identifying the relevant length scale(s) that best capture the growth in τ_α in the $T < T_c$ ($\phi > \phi_{\text{MCT}}$) regime²⁹, determining whether ξ_d is eventually slaved to ξ_{stat} is crucial. While this is presently beyond the scope of particle-resolved experiments, numerical studies that exploit the swap Monte Carlo technique may be the way forward^{46,47}. CRRs are a generic

feature of other competing theoretical frameworks of the glass transition as well and whether our observations can be reconciled within these approaches remains an open challenge. Finally, the very existence of such amorphous–amorphous interfaces opens up the possibility of tuning their properties, and hence that of the glass itself, in a manner analogous to grain boundary engineering in polycrystals⁴⁸.

Methods

Experimental details. Our experimental system comprises of a binary mixture of colloidal polystyrene particles with sizes $\sigma_s = 1.05 \mu\text{m}$ and $\sigma_l = 1.4 \mu\text{m}$, respectively. The number density ratio of big and small particles $N_l/N_s = 1.23$ is sufficient to prevent crystallization and is held nearly constant for all area fractions, ϕ , studied. Here, ϕ plays the role of an inverse temperature. Single-particle dynamics are studied using optical video microscopy. The colloidal suspensions are loaded in a wedge-shaped cell that is left standing for a suitable time duration to yield the desired particle area fraction ϕ . The systems are equilibrated for a typical time duration of 8–10 h before the experiments (several times τ_α for all ϕ s < 0.79). Samples are imaged using a Leica DMI 6000B optical microscope with a 100 \times objective (Plan apochromat, NA 1.4, oil immersion) and images are captured at frame rates ranging from 3.3 fps to 5 fps for 1–1.5 h depending on the values of ϕ . The typical field of view captured in our experiment is of the size $72\sigma_s \times 44\sigma_s$. The analysis reported here is carried out on experiments that were performed immediately after the holographic optical tweezers, that are used to pin an amorphous wall of particles, was turned off²¹ (Supplementary Note 3). Thus, a direct comparison of the present findings with the earlier study is justified. The particle trajectories are obtained from standard MATLAB algorithms⁴⁹. Subsequent analysis is performed using codes developed in-house. The typical drift observed in the experimental data in the presence of a pinned amorphous wall is of the order of $0.7\sigma_s$ in the x -direction and $0.15\sigma_s$ in the z -direction over the entire duration of the experiment. Since sample drift corrections are not possible in the presence of the wall, we choose the longest time window where the sample drift was $< 0.1\sigma_s$ for further analysis.

Data availability. The data that support the findings of this study are available from the corresponding author upon request.

Received: 28 August 2017 Accepted: 3 January 2018

Published online: 26 January 2018

References

- Berthier, L. & Biroli, G. Theoretical perspective on the glass transition and amorphous materials. *Rev. Mod. Phys.* **83**, 587 (2011).
- Gokhale, S., Sood, A. K. & Ganapathy, R. Deconstructing the glass transition through critical experiments on colloids. *Adv. Phys.* **65**, 363–453 (2016).
- Cavagna, A. Supercooled liquids for pedestrians. *Phys. Rep.* **476**, 51–124 (2009).
- Adam, L. & Gibbs, J. H. On the temperature dependence of cooperative relaxation properties in glass-forming liquids. *J. Chem. Phys.* **43**, 139–146 (1965).
- Kirkpatrick, T. R., Thirumalai, D. & Wolynes, P. G. Scaling concepts for the dynamics of viscous liquids near an ideal glassy state. *Phys. Rev. A* **40**, 1045 (1989).
- Kirkpatrick, T. R. & Thirumalai, D. Random first order transition theory concepts in biology and physics. *Rev. Mod. Phys.* **87**, 183 (2015).
- Tarjus, G., Kivelson, S. A., Nussinov, Z. & Viot, P. The frustration-based approach of supercooled liquids and the glass transition: a review and critical assessment. *J. Phys. Condens. Matter* **17**, R1143–R1182 (2005).
- Tanaka, H., Kawasaki, T., Shintani, H. & Watanabe, K. Critical-like behaviour of glass-forming liquids. *Nat. Mater.* **9**, 324–331 (2010).
- Leutheusser, E. Dynamical model of the liquid-glass transition. *Phys. Rev. A* **29**, 2765 (1984).
- Bengtzelius, U., Gotze, W. & Sjolander, A. Dynamics of supercooled liquids and the glass transition. *J. Phys. C* **17**, 5915 (1984).
- Keys, A. S. et al. Excitations are localized and relaxation is hierarchical in glass-forming liquids. *Phys. Rev. X* **1**, 021013 (2011).
- Lubchenko, V. & Wolynes, P. G. Theory of structural glasses and supercooled liquids. *Annu. Rev. Phys. Chem.* **58**, 235–266 (2007).
- Cammarota, C. et al. Evidence for a spinodal limit of amorphous excitations in glassy systems. *J. Stat. Mech. Theory Exp.* **12**, L12002 (2009).
- Zarinelli, E. & Franz, S. Surface tension in kac glass models. *J. Stat. Mech. Theory Exp.* **4**, P04008 (2010).
- Biroli, G. & Cammarota, C. Fluctuations and shape of cooperative rearranging regions in glass-forming liquids. *Phys. Rev. X* **7**, 011011 (2017).

16. Biroli, G. et al. Thermodynamic signature of growing amorphous order in glass-forming liquids. *Nat. Phys.* **4**, 771–775 (2008).
17. Gradenigo, G., Trozzo, R., Cavagna, A., Grigera, T. S. & Verrocchio, P. Static correlations functions and domain walls in glass-forming liquids: The case of a sandwich geometry. *J. Chem. Phys.* **138**, 12A509 (2013).
18. Cammarota, C., Cavagna, A., Gradenigo, G., Grigera, T. S. & Verrocchio, P. Numerical determination of the exponents controlling the relationship between time, length, and temperature in glass-forming liquids. *J. Chem. Phys.* **131**, 194901 (2009).
19. Stevenson, J. D., Schmalian, J. & Wolynes, P. G. The shapes of cooperatively rearranging regions in glass-forming liquids. *Nat. Phys.* **2**, 268–274 (2006).
20. Kob, W., Roldan-Vargas, S. & Berthier, L. Non-monotonic temperature evolution of dynamic correlations in glass-forming liquids. *Nat. Phys.* **8**, 164–167 (2012).
21. Nagamanasa, K. H., Gokhale, S., Sood, A. K. & Ganapathy, R. Direct measurements of growing amorphous order and non-monotonic dynamic correlations in a colloidal glass-former. *Nat. Phys.* **11**, 403–408 (2015).
22. Mishra, C. K. & Ganapathy, R. Shape of dynamical heterogeneities and fractional Stokes-Einstein and Stokes-Einstein-Debye relations in quasi-two-dimensional suspensions of colloidal ellipsoids. *Phys. Rev. Lett.* **114**, 198302 (2015).
23. Berthier, L. & Kob, W. Static point-to-set correlations in glass-forming liquids. *Phys. Rev. E* **85**, 011102 (2012).
24. Chakrabarty, S., Karmakar, S. & Dasgupta, C. Dynamics of glass forming liquids with randomly pinned particles. *Sci. Rep.* **5**, 12577 (2015).
25. Cammarota, C. & Biroli, G. Ideal glass transitions by random pinning. *Proc. Natl Acad. Sci. USA* **109**, 8850–8855 (2012).
26. Ozawa, M., Kob, W., Ikeda, A. & Miyazaki, K. Equilibrium phase diagram of a randomly pinned glass-former. *Proc. Natl Acad. Sci. USA* **112**, 6914–6919 (2015).
27. Berthier, L. et al. Finite-size effects in the dynamics of glass-forming liquids. *Phys. Rev. E* **86**, 031502 (2012).
28. Flenner, E. & Szamel, G. Dynamic heterogeneities above and below the mode-coupling temperature: evidence of a dynamic crossover. *J. Chem. Phys.* **138**, 12A523 (2013).
29. Flenner, E. & Szamel, G. Characterizing dynamic length scales in glass-forming liquids. *Nat. Phys.* **8**, 696–697 (2012).
30. Kob, W., Roldan-Vargas, S. & Berthier, L. Reply to characterizing dynamic length scales in glass-forming liquids. *Nat. Phys.* **8**, 697 (2012).
31. Mei, B. et al. Nonmonotonic dynamic correlations in quasi-two-dimensional confined glass-forming liquids. *Phys. Rev. E* **95**, 050601 (2017).
32. Benjamin, R. & Horbach, J. Excess free energy of supercooled liquids at disordered walls. *Phys. Rev. E* **90**, 060101 (2014).
33. Jack, R. L. & Fullerton, C. J. Dynamical correlations in a glass former with randomly pinned particles. *Phys. Rev. E* **88**, 042304 (2013).
34. Kob, W. & Coslovich, D. Nonlinear dynamic response of glass-forming liquids to random pinning. *Phys. Rev. E* **90**, 052305 (2014).
35. Russo, J. & Tanaka, H. Assessing the role of static length scales behind glassy dynamics in polydisperse hard disks. *Proc. Natl Acad. Sci. USA* **112**, 6920–6924 (2015).
36. Yaida, S. et al. Point-to-set lengths, local structure, and glassiness. *Phys. Rev. E* **94**, 032605 (2016).
37. Penfold, J. The structure of the surface of pure liquids. *Rep. Prog. Phys.* **64**, 777 (2001).
38. Aarts, D. G. A. L., Schmidt, H. & Lekkerkerker, H. N. W. Direct visual observation of thermal capillary waves. *Science* **304**, 847–850 (2004).
39. Hernandez-Guzman, J. & Weeks, E. R. The equilibrium intrinsic crystal-liquid interface of colloids. *Proc. Natl Acad. Sci. USA* **106**, 15198–15202 (2009).
40. Skinner, T. O. E., Aarts, D. G. A. L. & Dullens, R. P. A. Grain-boundary fluctuations in two-dimensional colloidal crystals. *Phys. Rev. Lett.* **105**, 168301 (2010).
41. Gokhale, S., Nagamanasa, K. H., Sood, A. K. & Ganapathy, R. Directional grain growth from anisotropic kinetic roughening of grain boundaries in sheared colloidal crystals. *Proc. Natl Acad. Sci. USA* **109**, 20314–20319 (2012).
42. Donati, C., Glotzer, S. C., Poole, P. H., Kob, W. & Plimpton, S. J. Spatial correlations of mobility and immobility in a glass-forming Lennard-Jones liquid. *Phys. Rev. E* **60**, 3107 (1999).
43. Stevenson, J. D. & Wolynes, P. G. A universal origin for secondary relaxations in supercooled liquids and structural glasses. *Nat. Phys.* **6**, 62 (2009).
44. Weeks, E. R. et al. Three-dimensional direct imaging of structural relaxation near the colloidal glass transition. *Science* **287**, 627–631 (2000).
45. Nagamanasa, K. H., Gokhale, S., Ganapathy, R. & Sood, A. K. Confined glassy dynamics at grain boundaries in colloidal crystals. *Proc. Natl Acad. Sci. USA* **108**, 11323–11326 (2011).
46. Grigera, T. S. & Parisi, G. Fast Monte Carlo algorithm for supercooled soft spheres. *Phys. Rev. E* **63**, 045102 (2001).
47. Berthier, L. et al. Configurational entropy measurements in extremely supercooled liquids that break the glass ceiling. *Proc. Natl Acad. Sci. USA* **114**, 11356–11361 (2017).
48. Gottstein, G. & Shvindlerman, L.S. *Grain Boundary Migration In Metals: Thermodynamics, Kinetics, Applications*. 2nd ed. (CRC Press, 2009).
49. Crocker, J. C. & Grier, D. G. Methods of digital video microscopy for colloidal studies. *J. Colloid Interface Sci.* **179**, 298–310 (1996).

Acknowledgements

We thank Walter Kob for illuminating discussions and Francesco Sciortino for encouraging comments. We thank Shreyas Gokhale for the critical feedback on our manuscript. A.K.S. thanks Year of Science Fellowship of the Department of Science and Technology (DST), India, for support. R.G. thanks the ICMS and SSL, JNCASR for financial support and DST for a SwarnaJayanti Fellowship grant.

Author contributions

D.G., A.K.S., and R.G. conceived the research. H.K.N. performed the experiments. D.G. and R.G. developed the analysis procedures. D.G. performed the analysis. R.G. wrote the paper with inputs from all authors.


Additional information

Supplementary Information accompanies this paper at <https://doi.org/10.1038/s41467-018-02836-6>.

Competing interests: The authors declare no competing financial interests.

Reprints and permission information is available online at <http://npg.nature.com/reprintsandpermissions/>

Publisher's note: Springer Nature remains neutral with regard to jurisdictional claims in published maps and institutional affiliations.

 **Open Access** This article is licensed under a Creative Commons Attribution 4.0 International License, which permits use, sharing, adaptation, distribution and reproduction in any medium or format, as long as you give appropriate credit to the original author(s) and the source, provide a link to the Creative Commons license, and indicate if changes were made. The images or other third party material in this article are included in the article's Creative Commons license, unless indicated otherwise in a credit line to the material. If material is not included in the article's Creative Commons license and your intended use is not permitted by statutory regulation or exceeds the permitted use, you will need to obtain permission directly from the copyright holder. To view a copy of this license, visit <http://creativecommons.org/licenses/by/4.0/>.

© The Author(s) 2018